ChemComm

# All-In-One Sn-Co Alloy As Binder-Free Anode In High-Capacity Batteries And Its Dynamic Lithiation In Situ



| | |
|---|---|
| Journal: | *ChemComm* |
| Manuscript ID | CC-COM-10-2018-007868.R1 |
| Article Type: | Communication |
| | |

ChemComm

COMMUNICATION

# All-In-One Sn-Co Alloy As Binder-Free Anode In High-Capacity Batteries And Its Dynamic Lithiation *In Situ*

Received 00th January 20xx,
Accepted 00th January 20xx

DOI: 10.1039/x0xx00000x

www.rsc.org/

Jinyun Liu,*[#a] Ping Zhou,[#b] Wen Zhang,[a] Xi Chen,[c] Jiarui Huang,[a] Jinjin Li[d], Miaofang Chi,[e] and Junjie Niu*[c]

A three-dimensional all-in-one Sn-Co alloy anode is reported for the first time, which delivers a high capacity along with a stable Coulombic efficiency as well as a good temperature tolerance. The binder-free electrode eliminates the complexity of conventional slurry preparation while maintaining an integrated scaffold, which provides space to accommodate the volume expansion, as confirmed by *in situ* transmission electron microscopy study.

High energy-density secondary batteries have been of great interest in the emerging applications such as electric vehicles (EVs) and portable electronic devices.[1-5] Seeking alternatives that can deliver much higher capacity than the current graphite-based anodes is highly demanded. Metallic Sn is attracting more attention due to the almost 3x times higher capacity *via* alloying/dealloying reaction instead of intercalation.[6-8] To date tremendous efforts such as constructing porous structures and surface modifications have been made in preventing the large volume expansion.[9-13] B. Huang et al. reported a carbon encapsulated Sn-Co alloy composite which exhibits improved stability after 120 cycles.[14] Sn-Co alloy nanowires were prepared by Wang and co-workers through electrodeposition using $SnCl_2$-$CoCl_2$-EMIC ionic liquid, which exhibit specific capacities of about 654 mAh $g^{-1}$ after 60 cycles and 539 mAh $g^{-1}$ after 80 cycles at a current density of 300 mA $g^{-1}$.[15] Srinivas's group synthesized a $(Sn_{71}Co_{29})_{50}C_{50}$ composite by a combination of melt spinning and ball milling, and obtained consistent specific capacity of 387 mAh $g^{-1}$ for 35 cycles.[16] Intermetallic Co-Sn nanoparticles prepared by ball-milling showed a capacity of about 300 mAh $g^{-1}$ at 10C.[17] Yang et al presented a cubic yolk-shell structure with discrete Sn-Co nanoalloy[18]. In addition, many achievements indicate that Sn-Co alloy is a promising anode material.[19-21] However, the conventional methods usually introduce additional inactive materials that lead to a weak interaction with active materials. As a result, a rapid capacity decay was normally obtained,[22,23] which necessitates scientists to find a solution to reduce the additives and thus to retain a high capacity retention.

Herein, we reported a novel 3D scaffolded porous Sn-Co alloy anode, which exhibits the high specific capacity of 700 mAh $g^{-1}$ over 60 cycles and >630 mAh $g^{-1}$ over a hundred cycles. This good capacity retention is owed to the robust accommodation of the 3D porous scaffold upon lithiation/delithiation, which was observed using an *in-situ* transmission electron microscopy (TEM) technique.

The 3D Sn-Co alloy was synthesized through an opal-template-assisted method,[24,25] as illustrated in Fig. 1a. The experimental process with more details is shown in Supporting Information. At first, a 3D opal template was prepared on a tungsten substrate which was employed as current collector using ~300 nm polystyrene (PS) colloids via a self-assembly process (Fig. 1b and S1a, ESI†). An intermediate porous scaffold of $SnO_2$-$Co_3O_4$ (inverse opal) was generated after annealing the Sn (IV) and Co (II) precursors in the opal template (Fig. 1c and S2, ESI†). The final Sn-Co alloy with 3D configuration was formed via a $H_2$ reduction. The top-view and cross-section images of Sn-Co alloy elucidate a well-aligned porous 3D scaffold (similar to the ordered opal template in Fig. 1b), which contains plenty of spaces between the spherical units (Fig. 1d,e and S1b-d). The TEM morphologies in Fig. 1f and S3 (ESI†) further confirm the porous configuration. As seen from the high-resolution TEM (HRTEM) image, the lattice interspaces of 0.16 and 0.2 nm are indexed to the planes (101) and (312) of CoSn and $CoSn_3$, respectively (Fig. 1g).

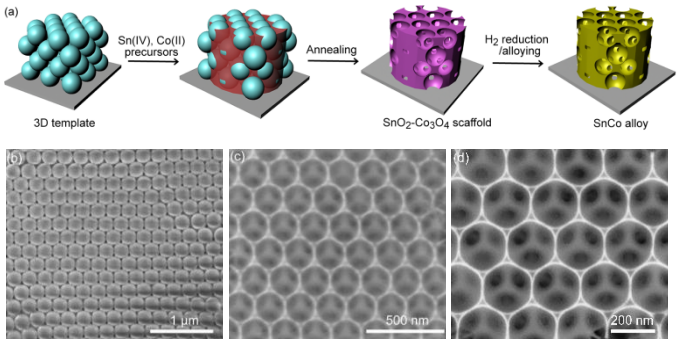


[a] Key Laboratory of Functional Molecular Solids, Ministry of Education, College of Chemistry and Materials Science, Anhui Normal University, Wuhu, Anhui 241002, P.R. China. E-mail: jyliu@iim.ac.cn
[b] Institute of Intelligent Machines, Chinese Academy of Sciences, Hefei 230031, P.R. China.
[c] Department of Materials Science and Engineering, University of Wisconsin-Milwaukee, Milwaukee, Wisconsin 53211, United States. E-mail: niu@uwm.edu
[d] Department of Micro/Nano Electronics, Shanghai Jiao Tong University, Shanghai 200240, P.R. China.
[e] Center for Nanophase Materials Sciences, Oak Ridge National Laboratory, Oak Ridge, Tennessee 37831, United States
[#] These authors contributed equally to this work.
† Electronic Supplementary Information (ESI) available: Experimental process, supplementary figures and movie. See DOI: 10.1039/x0xx00000x

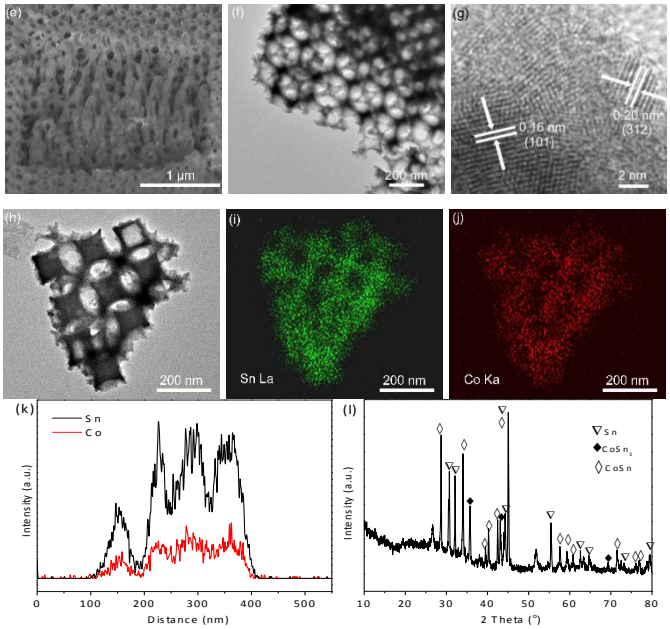


**Fig. 1** (a) Illustration of the 3D Sn-Co alloy preparation process. (b) SEM top-view images of the (b) PS opal, (c) $SnO_2$-$Co_3O_4$ inverse opal, and (d) Sn-Co alloy. (e) SEM image of the Sn-Co alloy after the focused ion beam radiation. (f) TEM and (g) HR-TEM images. TEM image (h) and elemental mappings of (i) Sn and (j) Co of the Sn-Co alloy. (k) Line-scanning profiles of Sn and Co at the location shown in (h). (l) XRD pattern of the Sn-Co alloy.

The elemental mappings (Fig. 1h-j), energy-dispersive spectrum (EDS, Fig. S4, ESI†) and line scanning maps of Sn and Co (Fig. 1k) show that the molar ratio of Sn:Co is about 5:1 within the Sn-Co alloy. In addition, the uniform distribution of elements Sn and Co along with periodical inter-spaces is confirmed. The XRD pattern in Fig. 1l confirms the majority of Sn-Co alloy phase with a small amount of Sn and $CoSn_3$ (JCPDS Nos. 48-1813, 02-0559, and 04-0673). The peaks at ~27° and ~52° are assigned to the crystal planes (110) and (211) of $SnO_2$ (JCPDS No. 41-1445), which may be formed due to the oxidization during XRD measurement. The binding energies of Sn $3d_{5/2}/3d_{1/2}$ at 486.7/495.1 eV and Co $2p_{3/2A}/2p_{1/2A}$ at 781.2/797.1 eV are identified from the Sn-Co alloy *via* the XPS analysis (Fig. S5, ESI†).[26] The Co $2p_{3/2B}/2p_{1/2B}$ at 786.5/802.1 eV are assigned to the cobalt (II) oxide species,[27] which is ascribed to the surface oxidization of the sample during the characterizations.

The electrochemical performance of the battery using the all-in-one Sn-Co alloy as anode, without additional slurry preparation and film-casting process, was checked. As shown in the CVs in Fig. 2a, the peak at ~0.7 V upon the first cathodic scan is ascribed to the formation of solid electrolyte interphase (SEI).[28] Single-phase Co-Sn alloys including $\alpha$-$CoSn_3$, $CoSn_2$, and CoSn, can act as anodes in Li-ion batteries.[29] For example, the $\alpha$-$CoSn_3$ alloy can directly transform into a $Li_xSn$ phase and Co particles.[30] The reversible plateau at about 0.2 to 0.6 V (*vs.* $Li/Li^+$) in the following cycles is due to the lithiation of Sn to form $Li_xSn$ ($xLi^+ + Sn + xe^- \leftrightarrow Li_{x(0<x<4.4)}Sn$) while the one upon anodic scan is due to the corresponding delithiation.[31-33] The peak at 1.0-1.3 V is originated from the reaction of $xCo + Li_{4.25}Sn \leftrightarrow Co_xSn + 4.25Li^+ + 4.25e^-$.[34,35] These redox peaks show a good agreement with the plateaus in the charge/discharge profiles (Fig. 2b) and differential capacity curves (Fig. S6, ESI†). The peak at ~1.5 V is assigned to the electrochemical reaction of partly oxidized Sn-Co alloys or carbon shell.[18,23] In addition, the XRD pattern (Fig. S7, ESI†) of the Sn-Co alloy after delithiation shows the $Co_3Sn_2$ phase, indicating an alloy product instead of a mixture of Co and Sn. For comparison, the CV curves of pure metal Sn and Co are shown in Fig. S8 (ESI†). The rate performance of the battery was tested under the rates ranging from 0.1 to 2.0 C (Fig. 2c and S9, ESI†). The specific capacity of 811, 782, 590, and 469 mAh $g^{-1}$ was received respectively. Particularly a recovered capacity of 678 $mAhg^{-1}$ at 0.1 C after a series of cycles indicates a high capacity retention up to 83.6%.

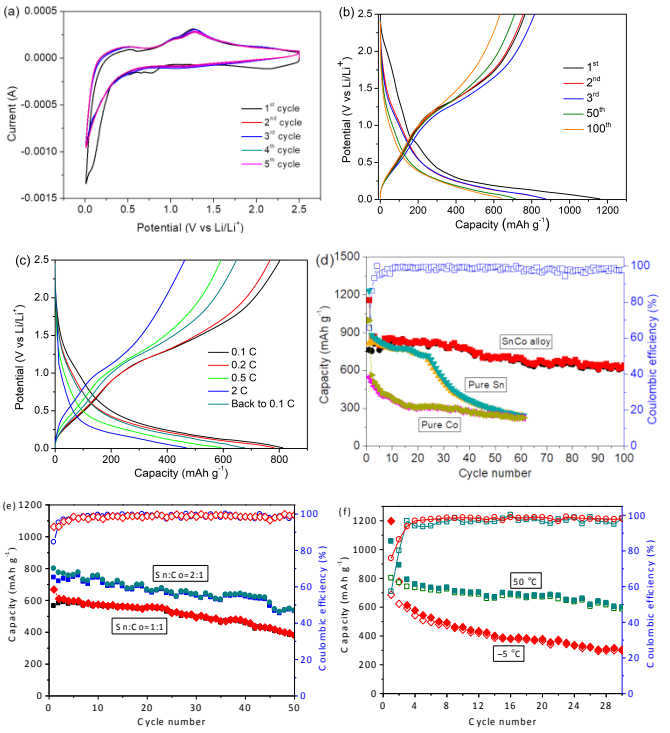


**Fig. 2** (a) CV curves of the battery using Sn-Co alloy as anode with the potential window between 0 to 2.5 V *vs.* $Li/Li^+$ at a scanning rate of 0.1 mV $s^{-1}$. (b) Galvanostatic charge/discharge profiles of the battery at 0.5 C. (c) Rate performance of the battery from 0.1 to 2 C, and back to 0.1 C. The data were collected every 10 cycles under each rate. (d) Cycling capability of the battery with Sn-Co alloy, pure Sn or Co scaffold at 0.5 C. The Coulombic efficiency is from the Sn-Co alloy battery. The molar ratio of Sn/Co in a-d is 5:1. (e) Cycling performance of the Sn-Co alloy batteries with different Sn/Co ratios of 1:1 and 2:1 at 0.5 C. (f) Temperature tolerance of the battery with a Sn/Co molar ratio of 5:1 under –5 °C and 50 °C at 0.2 C. The capacity of the binder-free anode was calculated based on the 'whole electrode' except the substrate tungsten.

As observed in Fig. 2d, the battery with Sn-Co alloy as anode delivers a high discharge capacity of 1159 mAh $g^{-1}$ at the first cycle under 0.5 C along with a CE of 65.8% due to the formation of SEI, and the reaction of Co with some $Li_2O$ on Li foil that can provide additional capacity.[36-40] The nanosized Co facilitates the decomposition of $Li_2O$ during the charging process, resulting in the more reversible reaction with less capacity loss.[41] The formed $Co_3O_4$ has a theoretical capacity of 890 mAh $g^{-1}$. In many cases, the practical capacity of Sn-Co will contain the contributions from both

 

Sn and $Co_3O_4$. A capacity of 700 mAh $g^{-1}$ with a CE of 98.7% after 60 cycles and 630 mAh $g^{-1}$ with a CE of 98.1% after 100 cycles were remained respectively, indicating a good capacity retention with negligible capacity loss. As the comparison, the battery using similar 3D inverse opal structure of pure Sn or Co (Fig. S10, ESI†) was also checked. As shown in Fig. 2d, the Sn anode provides a capacity of 810 mAh $g^{-1}$ initially, however, it drops to about 280 mAh $g^{-1}$ only after 60 cycles. In parallel, the pure Co displays a capacity of ~300 mAh $g^{-1}$ over 60 cycles. The reversible capacity is contributed from the reactions $3Co^0 + 4Li_2O \leftrightarrow Co_3O_4 + 8Li^+ + 8e^-$,[42] and $Co^0 + Li_2O \leftrightarrow CoO + 2Li^+ + 2e^-$.[43] These reactions have the high theoretical capacity of 700-1000 $mAhg^{-1}$.[44] It is known that over 300% volume expansion of Sn will occur during the lithiation that leads to severe pulverizations. The $Co_3O_4$ produced by metal Co shows a negligible volume change,[45-47] thus enabling a stable capacity retention of the Sn-Co alloy anode (Fig. 2d). In the all-in-one Sn-Co alloy, the porous Co scaffold as a robust frame base creates supporting sites with sufficient spaces to accommodate the volume change of Sn. The SEM images show that the original 3D configuration of the Sn-Co alloy after 60 cycles was remained (Fig. S11, ESI†). Electrochemical impedance spectroscopy analysis indicates that the charge-transfer resistance ($R_{ct}$) of the fresh Sn-Co anode was approximately 41.3 Ω, which was slightly lower than that after 60 cycles (Fig. S12, ESI†). This low impedance with high electrochemical stability upon cycling is ascribed to the metallic alloy structure and the tungsten substrate that provide a fast transport pathway with an improved conductivity of $Li^+/e^-$. As the result, a high specific capacity with a slight decay was achieved. In the control experiments, Sn-Co alloy film electrodes were fabricated with additives including carbon black and binders through a conventional slurry-based method. The initial capacity of about 600 mAh $g^{-1}$ is received while it rapidly decays to below 400 mAh $g^{-1}$. The additives in the electrode can destroy the 3D porous scaffold structure, and reduce the space to accommodate the volume change during lithiation/delithiation.

Through adjusting the amount of Sn (VI) and Co (II) precursors, a controllable Sn-Co alloy with a desirable Sn/Co ratio can be synthesized. Shown in Fig. 3e are the cycling profiles of the battery with Sn/Co molar ratios of 1:1 and 2:1, respectively. It is seen that the capacity was decreased from 600 to 400 mAh $g^{-1}$ when the Co ratio was increased, while an enhanced capacity retention was received. This improved cycling stability further confirms the role of Co in maintaining high electrochemical reliability of the alloy. In order to evaluate the temperature dependence, the battery with a Sn/Co molar ratio of 5:1 was cycled at a high temperature of 50 °C and a low temperature of –5 °C at 0.2 C, respectively (Fig. 2f). The high capacities of 587 and 301 mAh $g^{-1}$ were obtained at 50 and –5 °C after 30 cycles, respectively. The slight capacity fluctuation at 50 °C is believed due to the instability of electrolyte. The relatively high capacity retention at various temperatures demonstrates an improved charge transfer kinetics at both high and low temperatures that leads to broad applications of the batteries.

The real-time lithiation was investigated using *in-situ* TEM, since this technology enables electrochemical reaction being observed inside a TEM.[48] In our study, the experimental set-up of a nano-battery for *in-situ* TEM is shown in Fig. 3a. A piece of Sn-Co alloy was connected to the tip of Al wire tip using conductive epoxy. During the test, the sample was manipulated to contact a Li foil as counter electrode that was attached on a tungsten (W) tip, as shown in Fig. 3b. The liquid electrolytes including ionic liquid evaporate and wet the sample quickly under TEM conditions, which can lead to a poor resolution. In this study, the ultra-thin $Li_2O$ layer on Li foil was employed as a solid electrolyte instead. As seen from the morphology evolution in Fig. 3c, the Sn-Co alloy displays a gradually increased volume expansion after the lithium insertion from 0 to 60 seconds (red circle). The clear particle boundary (0 s) turned to be indistinct since the 2 s, indicating a rapid lithiation. During lithiation, the structure maintains 3D porous structure. No cracks, pulverizations and material loss were observed from the real-time images, indicating a well accommodation and a robust structure of the 3D Sn-Co alloy scaffold. In addition, the phase conversion from polycrystal to amorphous after the 60 seconds lithiation was identified from the fast Fourier transform (FFT) patterns (Fig. 3c insets), confirming the alloying reaction with lithium.[49] The dynamic lithiation process recorded by *in-situ* TEM is also shown in the Movie S1 (ESI†). The *in-situ* TEM investigation further confirms the 3D porous scaffold has a strong mechanical property and an enhanced capability of volume accommodation.

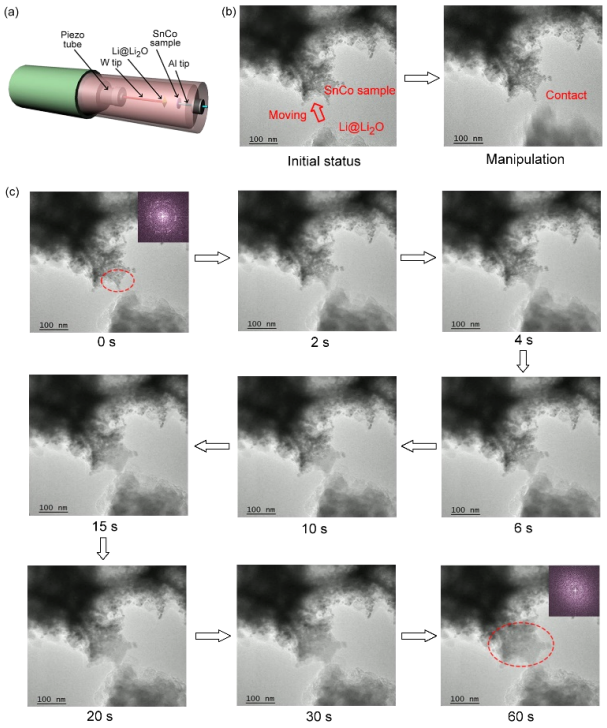


**Fig. 3** (a) Illustration of the in-situ TEM setup of a nano-battery using the Sn-Co alloy as anode. (b) TEM images of the sample at the initial position and after the manipulation. (c) Morphology evolution of the Sn-Co alloy from 0 to 60 seconds during lithiation. The insets in (c) are the corresponding FFT patterns.

In summary, we report a 3D Sn-Co alloy scaffold as all-in-one anode in LIBs. The high mechanical strength of the Co scaffold stabilized the overall electrode while providing enough space to accommodate the volume variation of Sn, which was demonstrated using *in situ* TEM. Compared to pure Sn and Co with the same 3D scaffolded structure, the Sn-Co alloy anode shows an improved performance. The battery with improved capacity, rate capability,

temperature tolerance, and simple process without additives displays great potential in powering potable electronic devices.

This work was supported by the National Natural Science Foundation of China (51672176, 21471005, and 661573334), the Major Project of the Department of Education of Anhui Province (KJ2018ZD034), the Creative Science Foundation of AHNU (2018XJJ108), the Science Foundation for Talent of AHNU (751707). The *in situ* TEM observations were performed by the user facility at the Center for Nanophase Materials Science, Oak Ridge National Laboratory (ORNL).

## Conflicts of interest

There are no conflicts to declare.

## Notes and references

1 J. M. Tarascon, M. Armand, *Nature* 2001, **414**, 359.
2 F. T. Wagner, B. Lakshmanan, M. F. Mathias, *J. Phys. Chem. Lett.* 2010, **1**, 2204.
3 M. Winter, J. O. Besenhard, M. E. Spahr, P. Novak, *Adv. Mater*. 1998, **10**, 725.
4 B. Dunn, H. Kamath, J. M. Tarascon, *Science* 2011, **334**, 928.
5 L. Lu, X. Han, J. Li, J. Hua, M. Ouyang, *J. Power Sources* 2013, **226**, 272.
6 Y. Idota, T. Kubota, A. Matsufuji, Y. Maekawa, T. Miyasaka, *Science* 1997, **276**, 1395.
7 B. L. Ellis, K. T. Lee, L. F. Nazar, *Chem. Mater.* 2010, **22**, 691.
8 H. Shi, Z. Fang, X. Zhang, F. Li, Y. Tang, Y. Zhou, P. Wu, G. Yu, *Nano Lett.* 2018, **18**, 3193.
9 T. L. Lee, R. A. Adams, C. Luhrs, A. Arora, V. G. Pol, C.-H. Wu, J. Phillips, *Carbon* 2018, **132**, 411.
10 Y. Xu, Y. Zhu, Y. Liu, C. Wang, *Adv. Energy Mater.* 2013, **3**, 128.
11 Y. Guo, X. Zeng, Y. Zhang, Z. Dai, H. Fan, Y. Huang, W. Zhang, H. Zhang, J. Lu, F. Huo, Q. Yan, *ACS Appl. Mater. Interfaces* 2017, **9**, 17173.
12 M. G. Park, D. H. Lee, H. Jung, J. H. Choi, C. M. Park, *ACS Nano* 2018,**12**,2955.
13 M. Srinivas, A. S. Kumar, B. Majumdar, L. Neelakantan, *Mater. Today Commun.* 2017, **13**, 53.
14 B. Huang, J. Yang, Y. Li, S. Xiao, Q. Chen, *Mater. Lett.* 2018, **210**, 321-324.
15 L. P. Wang, G. Chen, Q. X. Shen, G. M. Li, S. Y. Guan, B. Li, *Int. J. Min. Met. Mater.* 2018, **25**, 1027.
16 M. Srinivas, A. S. Kumar, B. Majumdar, L. Neelakantan, *Mater. Today Commun.* 2017, **13**, 53.
17 M. Walter, S. Doswald, F. Krumeich, M. He, R. Widmer, N. P. Stadie, M. V. Kovalenko, *Nanoscale* 2018, **10**, 3777.
18 J. Yang, J. Zhang, X. Zhou, Y. Ren, M. Jiang, J. Tang, *ACS Appl. Mater. Interfaces* 2018, doi: 10.1021/acsami.8b12242.
19 Y. Tang, C. Bi, D. Zhang, G. Hou, H. Cao, L. Wu, G. Zheng, Q. Wu, *Micropor. Mesopor. Mat.* 2019, **274**, 76.
20 W. Dong, D. Shen, S. Yang, B. Liang, X. Wang, Y. Liu, S. Li, *Chem. Rese. Chinese U.* 2018, **34**, 235.
21 X. Shi, H. Song, A. Li, X. Chen, J. Zhou, Z. Ma, *J. Mater. Chem. A* 2017, **5**, 5873.
22 J. B. Goodenough, Y. Kim, *J. Power Sources* 2011, **196**, 6688.
23 N. Nitta, F. Wu, J. T. Lee, G. Yushin, *Mater. Today* 2015, **18**, 252.
24 J. Liu, Q. Zheng, M. D. Goodman, H. Zhu, J. Kim, N. A. Krueger, H. Ning, X. J. Huang, J. H. Liu, M. Terrones, P. V. Braun, *Adv. Mater.* 2016, **28**, 7696.
25 J. Y. Liu, J. Wang, J. Kim, H. L. Ning, Z. Pan, S. J. Kelly, E. S. Epstein, J. H. Liu, M. Terrones, P. V. Braun, *Small* 2015, **11**, 6241.
26 J. T. Li, J. Swiatowska, A. Seyeux, L. Huang, V. Maurice, S. G. Sun, P. Marcus, *J. Power Sources* 2010, **195**, 8251.
27 R. Dedryvère, S. Laruelle, S. Grugeon, P. Poizot, D. Gonbeau, J. M. Tarascon, *Chem. Mater.* 2004, **16**, 1056.
28 B. Liu, A. Abouimrane, M. Balasubramanian, Y. Ren, K. Amine, *J. Phys. Chem. C* 2014, **118**, 3960.
29 Z. Yi, Z. M. Wang, Y. Cheng, L. M. Wang, *Energy Environ. Mater.* 2018, **1**, 132.
30 C. X. Zhai, N. Du, H. Zhang, J. X. Yu, P. Wu, C. M. Xiao, D. R. Yang, *Nanoscale* 2011, **3**, 1798.
31 C. L. Lee, D. H. Nam, J. Y. Eom, H. S. Kwon, Electron. *Mater. Lett*. 2016, **12**, 622.
32 A. D. W. Todd, P. P. Ferguson, M. D. Fleischauer, J. R. Dahn, *Inter. J. Energy Res.* 2010, **34**, 535.
33 T. Momma, M. Jeong, T. Yokoshima, H. Nara, A. Toyoda, T. Osaka, *J. Power Sources* 2013, **222**, 526.
34 J. Hassoun, S. Panero, G. Mulas, B. Scrosati, *J. Power Sources* 2007, **171**, 928.
35 J. Shin, W. H. Ryu, K. S. Park, I. D. Kim, *ACS Nano* 2013, **7**, 7330.
36 S. S. Zhang, *J. Power Sources* 2006, **162**, 1379.
37 J. B. Goodenough, Y. Kim, *Chem. Mater.* 2010, **22**, 587.
38 L. J. Fu, H. Liu, C. Li, Y. P. Wu, E. Rahm, R. Holze, H. Q. Wu, *Solid State Sci.* 2006, **8**, 113.
39 V. Etacheri, C. N. Hong, J. L. Tang, V. G. Pol, *ACS Appl. Mater. Interfaces* 2018, **10**, 4652. M. V. Reddy, G. Prithvi, K. P. Loh, B. V. R. Ch, *ACS Appl. Mater. Interfaces* 2014, **6**, 680.
40 H. Tabassum, R. Zou, A. Mahmood, Z. Liang, Q. Wang, H. Zhang, S. Gao, C. Qu, W. H. Guo, S. J. Guo, *Adv. Mater.* 2018, 1705441.
41 S. S. Chu, C. Yang, X. Xia, J. D. Wang, Y. L. Hou, X. T. Su, *New J. Chem.* 2016, **40**, 2722.
42 Y. Q. Zhang, Y. W. Wu, Y. H. Chu, L. Li, Q. P. Yu, Y. F. Zhu, G. Liu, Q. Hou, R. H. Zeng, L. Z. Zhao, *Electrochim. Acta* 2016, **188**, 909.
43 F. Wang, H. Y. Zhuo, X. G. Han, W. M. Chen, D. Sun, *J. Mater. Chem. A* 2017, **5**, 22964.
44 G. Liu, J. Shao, *J. Mater. Chem. A* 2017, **5**, 9801.
45 Y. Gu, F. Wu, Y. Wang, *Adv. Funct. Mater.* 2013, **23**, 893.
46 V. O. Golub, V. A. Lvov, I. Aseguinolaza, O. Salyuk, D. Popadiuk, Y. Kharlan, G. N. Kakazei, J. P. Araujo, J. M. Barandiaran, V. A. Chernenko, *Phys. Rev. B* 2017, **95**, 1983.
47 Q. Su, D. Xie, J. Zhang, G. H. Du, B. S. Xu, *ACS Nano* 2013, **7**, 9115.
48 J. Qin, D. Liu, X. Zhang, N. Zhao, C. Shi, E. Z. Liu, F. He, L. Ma, Q. Li, J. Li, C. He, *Nanoscale* 2017, **9**, 15856.
49 S. Wang, M. He, M. Walter, F. Krumeich, K. V. Kravchyk, M. V. Kovalenko, *Nanoscale* 2018, **10**, 6827.

 

# Table of Contents:

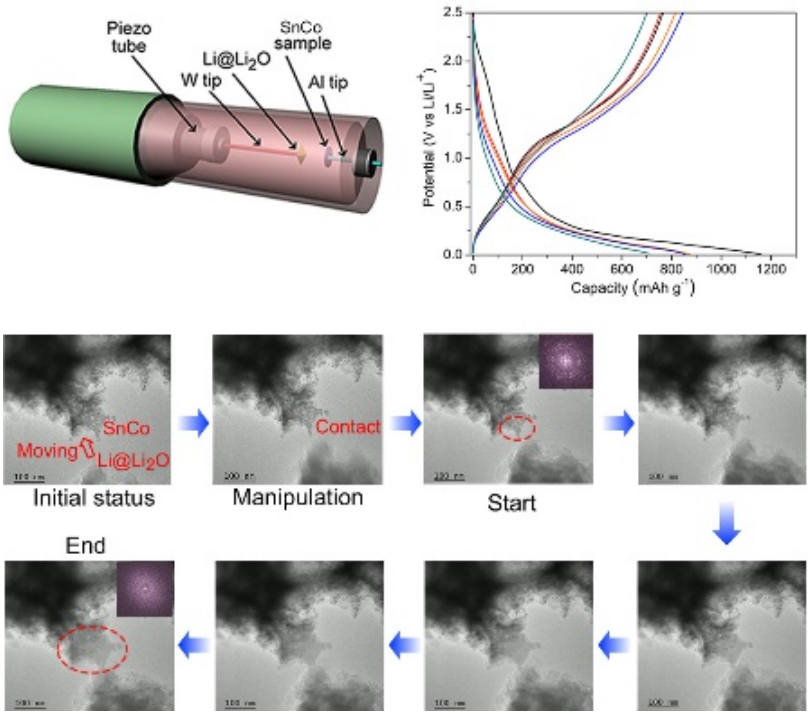


All-in-one Sn-Co alloy anode is reported, which exhibits robust electrode structure confirmed by *in situ* transmission electron microscopy.